Supplementary Information

Decoupling of ion pairing and ion conduction in ultrahigh-concentration electrolytes enables wide-temperature solid-state batteries

Shengjun Xu,‡[ab] Ruogu Xu,‡[ab] Tong Yu,[a] Ke Chen,[ac] Chengguo Sun,[ad] Guangjian Hu,[a] Shuo Bai,[ab] Hui-Ming Cheng,[ae] Zhenhua Sun[ab] and Feng Li*[ab]*

a Shenyang National Laboratory for Materials Science, Institute of Metal Research, Chinese Academy of Sciences, Shenyang 110016, China.

b School of Materials Science and Engineering, University of Science and Technology of China, Shenyang 110016, China.

c School of Physical Science and Technology, Shanghai Tech University, Shanghai 201210, China.

d School of Chemical Engineering, University of Science and Technology Liaoning, Anshan 114051, China.

e Faculty of Materials Science and Engineering/Institute of Technology for Carbon Neutrality, Shenzhen Institute of Advanced Technology, Chinese Academy of Sciences, Shenzhen 518055, China.

These authors contributed equally: Shengjun Xu, Ruogu Xu.

E-mail: zhsun@imr.ac.cn, fli@imr.ac.cn.

Experimental Section

Materials: DMSO was obtained from Sinopharm Chemical Regent Company. LiTFSI was purchased from Dodo Chem. PVDF-HFP was purchased from Sigma-Aldrich. All the chemicals were directly used as received.

Preparation of DMSO-based Liquid Electrolytes: Five electrolytes with different concentrations of LiTFSI salt in DMSO solvent (1 M, 3 M, 6 M, 9 M, and 12 M) were prepared by dissolving salt into the solvents and stirring in a glove box.

Preparation of S-LHCE: PVDF-HFP and LiTFSI (3:2 weight ratio) were dissolved in DMSO. The solution was cast onto a horizontal Teflon plate and freeze at -18 °C for 24 h. The pre-freezing sample was freeze dried for at least 48h.

Cathode and cell preparation: LFP cathodes were prepared by mixing LFP, Super P carbon (conductivity aid), PVDF (binder) and Homo-SPE [1] (solid-state electrolyte) at a weight of 7:1:1:1 in NMP solvent to form a smooth slurry and then painted on carbon-coated aluminum foils and dried in a vacuum oven to remove the NMP solvent. NCM811 cathodes were prepared by a similar procedure. The LFP and NCM811 loading were about 1-2 mg cm^{-2}. Coin 2025-type cells were assembled using a cathode, liquid electrolyte (40 µl) or S-LHCE, and lithium metal inside an argon-filled glovebox (LFP, 1C=170 mAh g^{-1}; NCM811, 1C=180 mAh g^{-1}).

Electrochemical measurements: Electrochemical measurements were carried out on an electrochemical station (Biologic VSP-300). The ionic conductivity was measured by electrochemical impedance spectroscopy (EIS) with a frequency range from 0.1Hz to 1M Hz and an amplitude voltage of 10 mV. A corresponding cell was assembled using two polished stainless-steel blocking electrodes in a glove box under an argon atmosphere. The ionic conductivity σ was calculated from the following equation:

$$\sigma = \frac{d}{S \times R} \quad (1)$$

where d and S are the area of and space between the electrodes, respectively, and R is the resistance. The electrochemical stability window was obtained at room temperature by linear sweep voltammetry (LSV) using stainless-steel as the working electrode and a lithium metal as the counter electrode at a scan rate of 0.5 mV s^{-1}. The Li^+ transference number (t_+) was measured by a

chronoamperometry test on a Li||Li cell with an applied voltage of 10 mV. On the basis of the measured values, t_+ was calculated by the following equation:

$$t_+ = \frac{I_s(\Delta V - I_0 R_0)}{I_0(\Delta V - I_s R_s)} \quad (2)$$

where ΔV is the applied bias, and the initial (I_0) and steady-state (I_s) currents are obtained from the chronoamperometric curve. R_0 and R_s measured by EIS, reflect the initial and steady-state resistances. The Coulombic efficiency test was carried out on Li||Cu cells, lithium plating and stripping were calculated from the ratio of the lithium removed from the Cu substrate to that deposited in the same cycle.

Characterization: ATR-FTIR spectra were recorded on a Nicolet iS5 iD7 ATR spectrometer equipped with a diamond KBr beam splitter and an empty ATR cell blanketed with argon was used to collect the background spectrum. The morphology of the samples was characterized by SEM (Verios G4 UC). Thermogravimetric analysis (TGA) and differential scanning calorimetry (DSC) were performed with a NETZSCH STA 449 C thermo balance in argon with a heating rate of 10 °C min^{-1} from room temperature to 600 °C. XPS analysis was performed using an ESCALAB 250 instrument with Al Kα radiation (15 kV, 150 W) under a pressure of 4×10^{-8} Pa. Raman spectroscopy was obtained using a Witec alpha300R with a 633 nm laser.

Computational simulation: The structure relaxations and properties calculations were carried out by spin-polarized density functional theory method, within the generalized gradient approximation of Perdew-Burke-Ernzerhof (GGA-PBE)[2,3] as implemented in the Vienna ab initio simulation package (VASP).[4] The ion-electron interaction was treated by the projector augmented wave (PAW) technique.[5] The plane-wave cutoff energy of 500 eV was employed. The atomic positions were fully relaxed until the maximum force on each atomic was less than 10^{-2} eV/Å. The Brillouin zone was sampled using the Monkhorst-Pack scheme with a k-point mesh of 3×3×1 in the Gamma-centered grids for structural relaxation. Van der Waals interaction was taken into account using the semiempirical DFT-D2 approach. A vacuum distance of ~20 Å was used to avoid interaction between adjacent layers. The binding energies in two-component systems are defiend by equation:

$$E_{binding} = E_{c1+c2} - E_{c1} - E_{c2} \quad (3)$$

Where $Ec_{1+}c_2$ are the total energies of two-component system by the hydrogen-bond-like interaction, Ec_1 and Ec_2 are the energies of used isolated components, respectively.

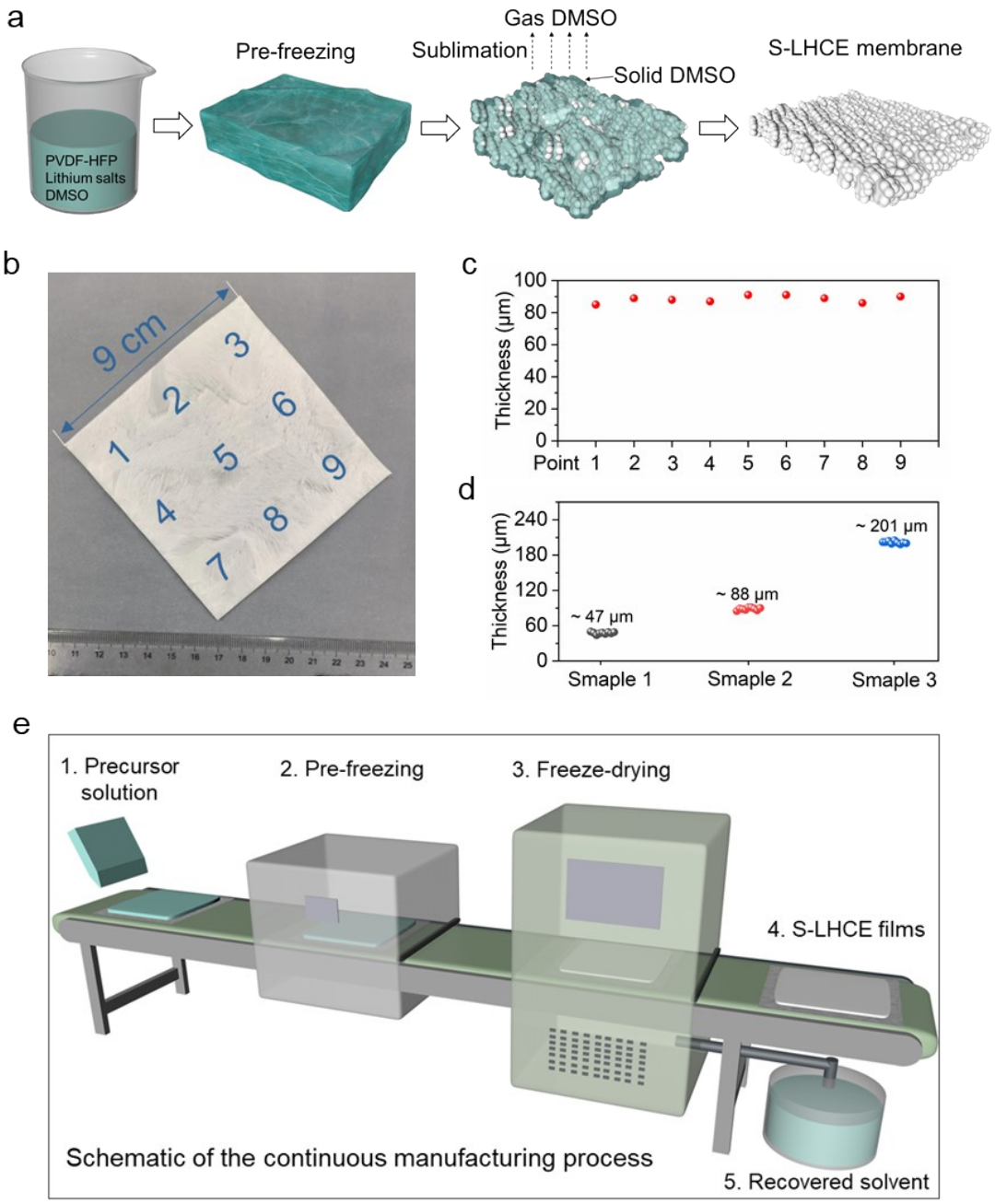

Supplementary Fig. 1. (a) The formation process of S-LHCE with particles morphology by freeze-drying method. (b) Photo of the prepared S-LHCE film. (c) Measured thickness at nine selected points in the prepared S-LHCE film. (d) Prepared S-LHCE films with controllable thickness. (e) Schematic of the continuous manufacturing process of the S-LHCE films by the freeze-drying method.

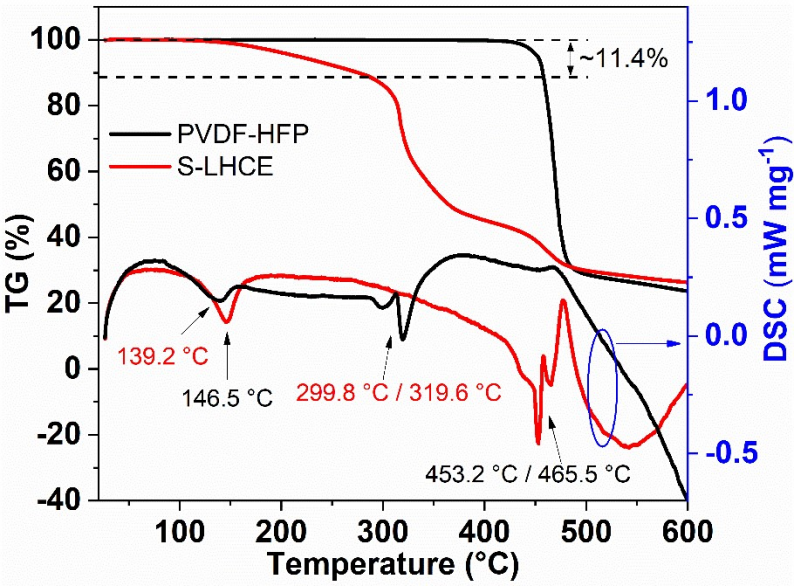

Supplementary Fig. 2. The TGA and DSC plots of S-LHCE and PVDF-HFP with a heating rate of 10 °C min^{-1} from room temperature to 600 °C under argon atmosphere.

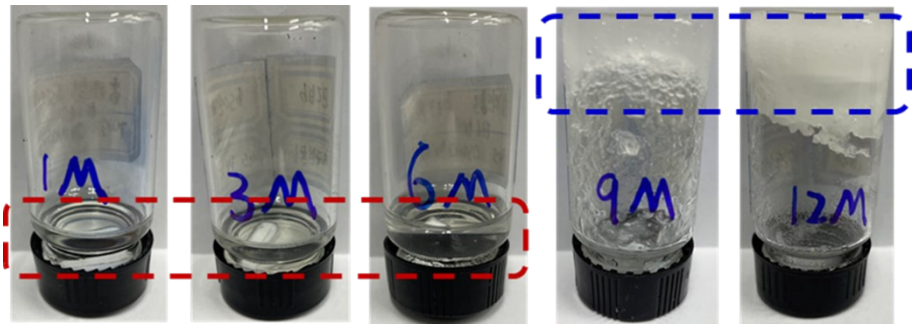

Supplementary Fig. 3. Photograph of 1 M, 3 M, 6 M, 9 M and 12 M liquid electrolytes.

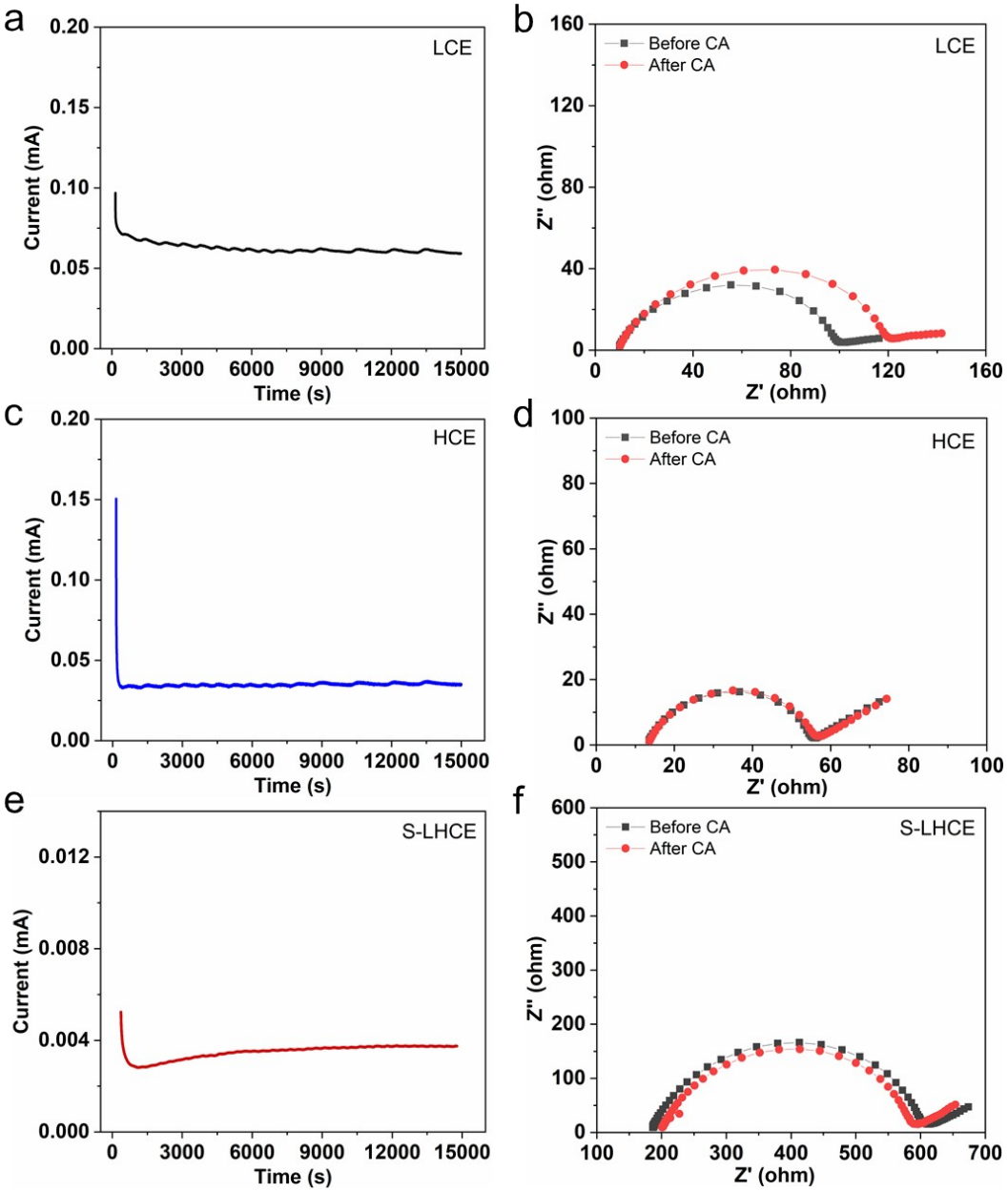

Supplementary Fig. 4. Li^+-transference number measurements of LCE (a, b), HCE (c, d) and S-LHCE (e, f). (a, c, e) Polarization (10 mV) curves of different electrolytes. (b, d, f) Electrochemical impedance spectra of different electrolytes before and after polarization.

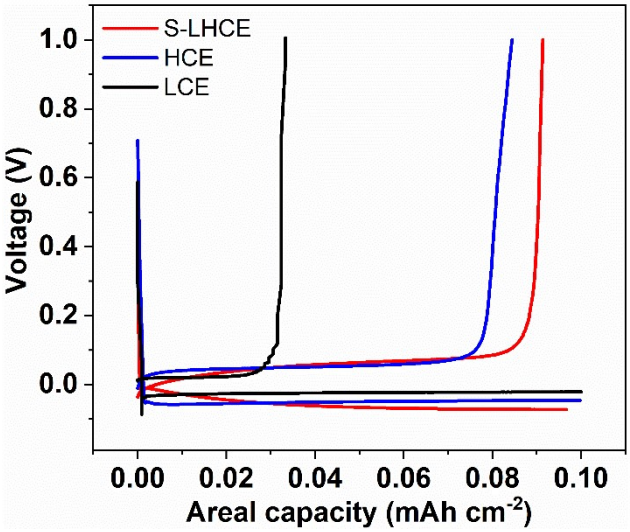

Supplementary Fig. 5. Voltage profiles of lithium plating/stripping in the Li||Cu cells with LCE, HCE and S-LHCE at 0.1 mA cm^{-2}.

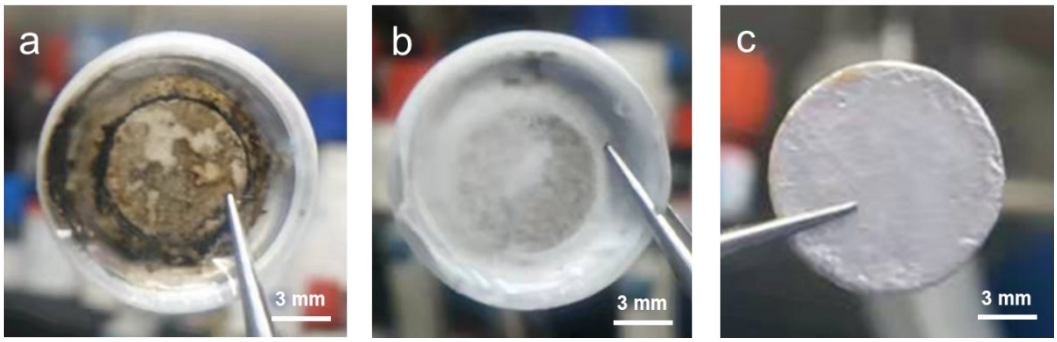

Supplementary Fig. 6. Optical images of cycled lithium metal in the LCE (a), HCE (b) and S-LHCE (c).

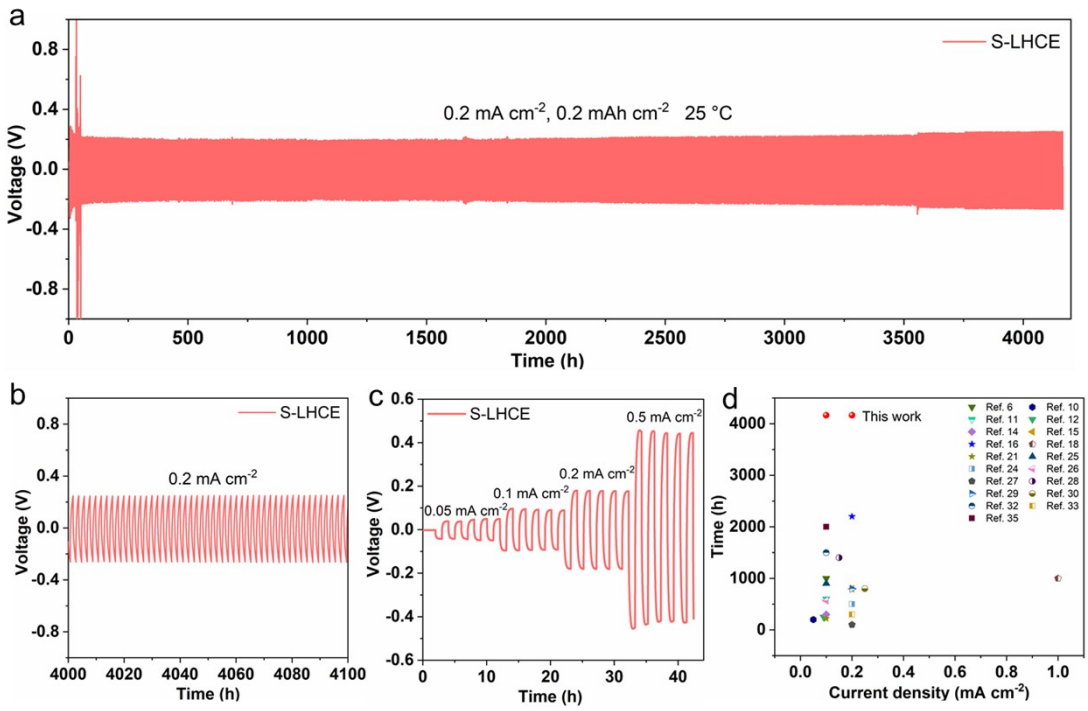

Supplementary Fig. 7. (a) Long-term cycling of symmetrical lithium cells using S-LHCE at 0.2 mA cm^{-2}. (b) The detailed voltage profiles of the symmetric cells at 0.2 mA cm^{-2} during 4000-4100 h. (c) Rate performance of symmetric lithium cells using S-LHCE under different current densities. (d) Comparison of cycling performance in symmetric lithium cells with various polymer electrolytes reported recently.

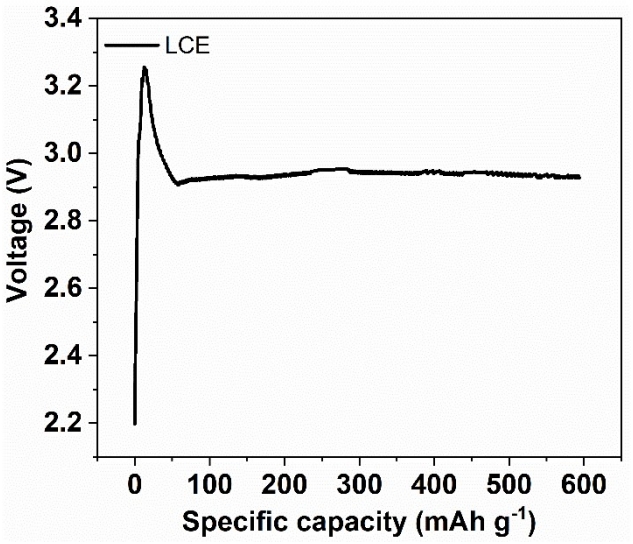

Supplementary Fig. 8. Voltage profile of the NCM811|LCE|Li cell.

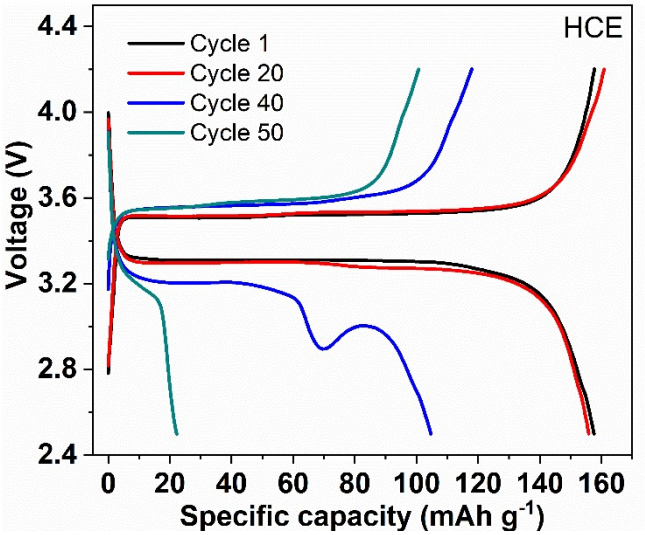

Supplementary Fig. 9. Voltage profile of the LFP|HCE|Li cell.

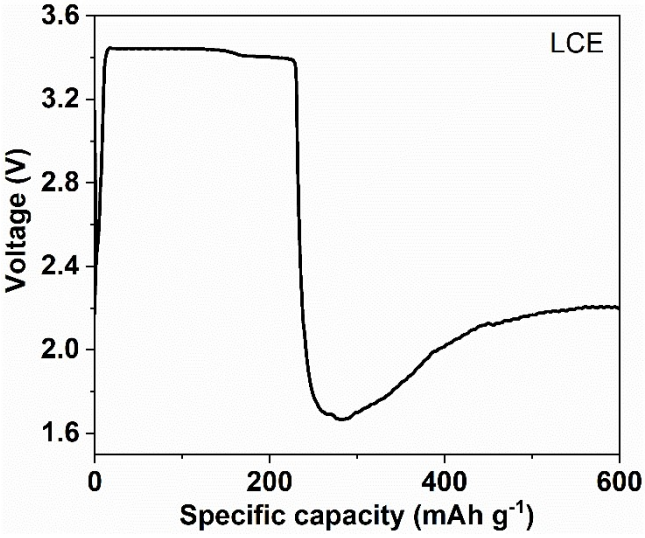

Supplementary Fig. 10. Voltage profile of the LFP|LCE|Li cell.

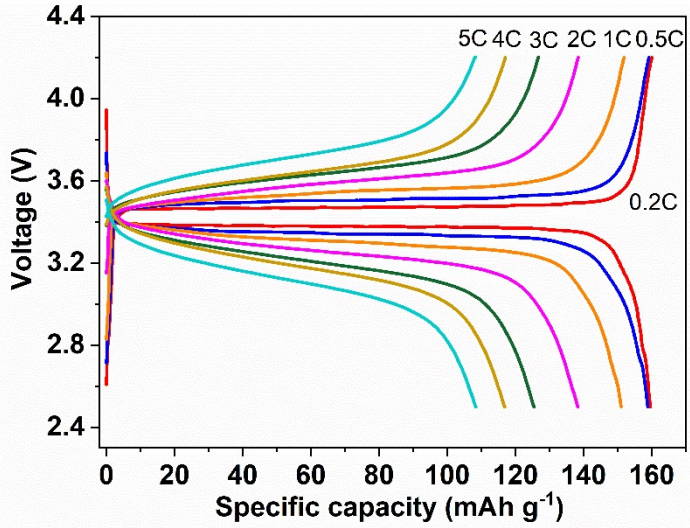

Supplementary Fig. 11. Voltage profiles of the LFP|S-LHCE|Li cell at different rates and room temperature.

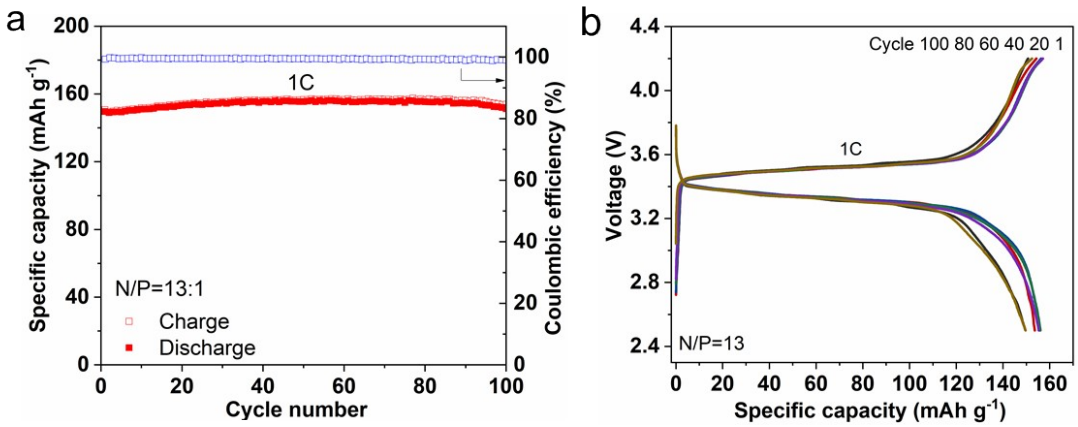

Supplementary Fig. 12. (a) Cycling performance of LFP|S-LHCE|Li full cell at room temperature and 1C. (b) Voltage profiles of the LFP|S-LHCE|Li full cell.

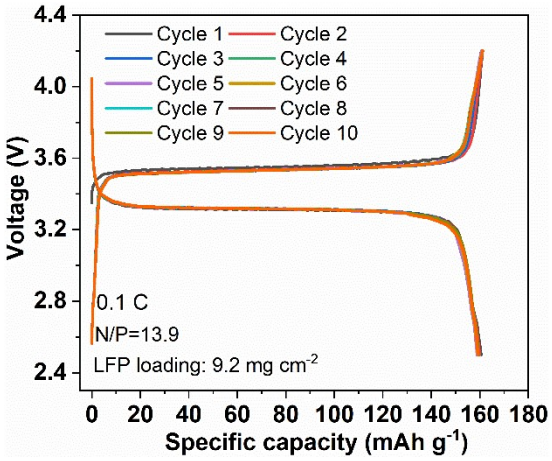

Supplementary Fig. 13. Voltage profiles of the LFP|S-LHCE|Li full cell with high cathode loading at 25 °C.

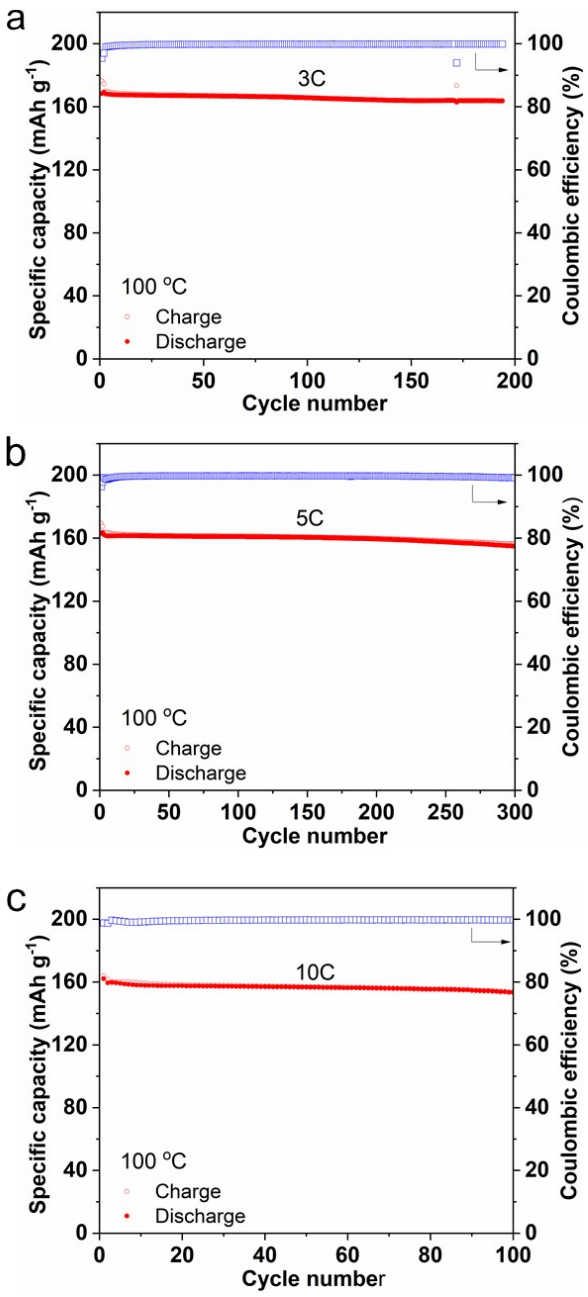

Supplementary Fig. 14. Cycling performance of LFP|S-LHCE|Li cells at 100 °C and 3 C (a), 5 C (b), and 10 C (c).

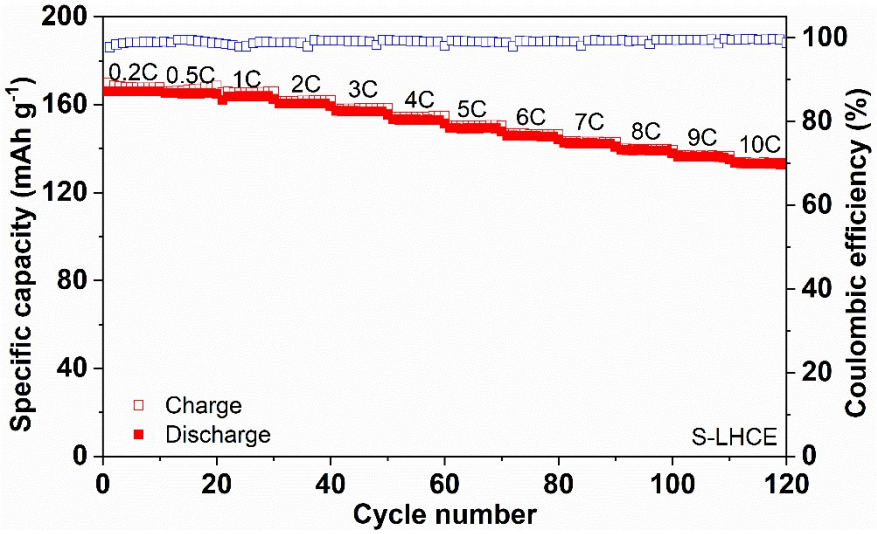

Supplementary Fig. 15. Rate performance of LFP|S-LHCE|Li cell at 50 °C.

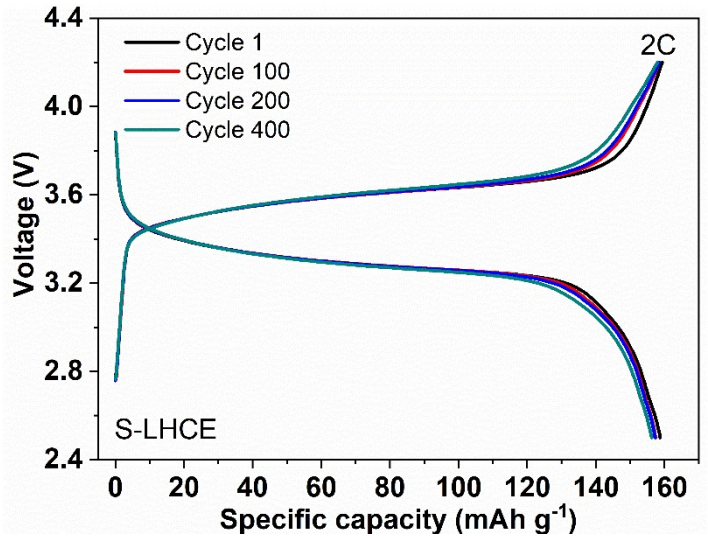

Supplementary Fig. 16. Voltage profiles of the LFP|S-LHCE|Li cell at different cycles at 35 °C.

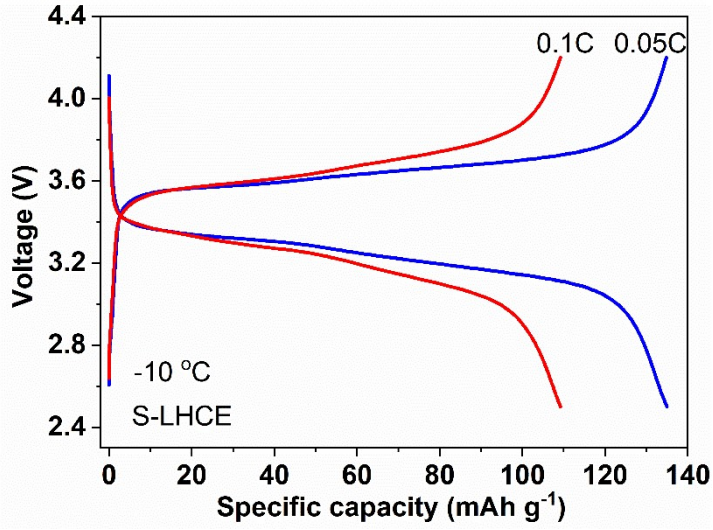

Supplementary Fig. 17. Voltage profiles of the LFP|S-LHCE|Li cell at different rates at -10 °C.

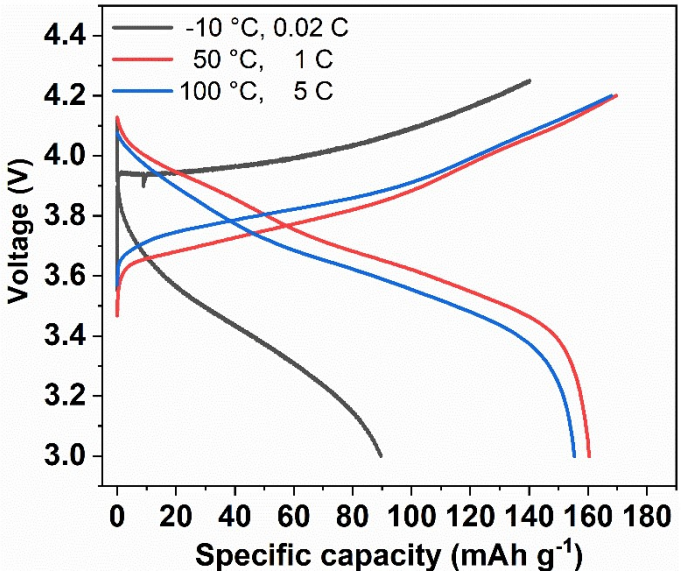

Supplementary Fig. 18. Voltage profiles of the NCM811|S-LHCE|Li cell at different temperatures.

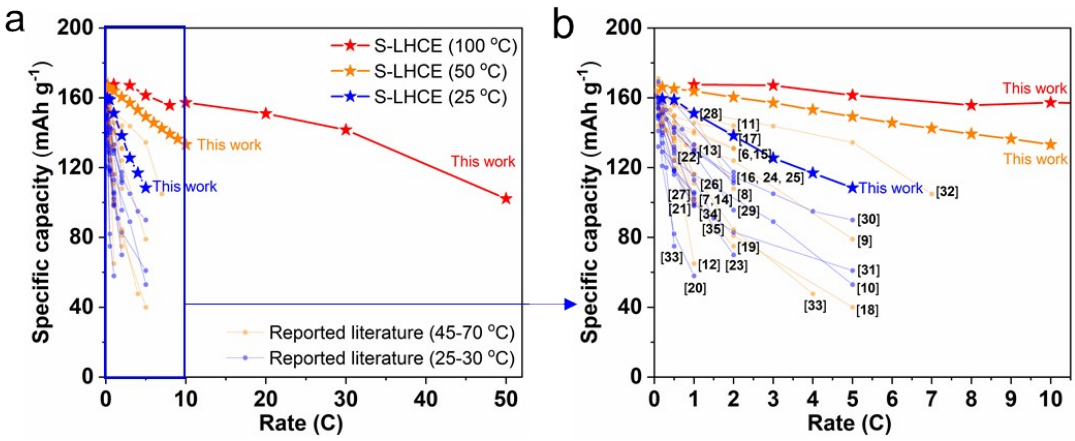

Supplementary Fig. 19. Comparison of rate performance for different polymer electrolytes in LFP||Li cells (a), and enlarged region (b).

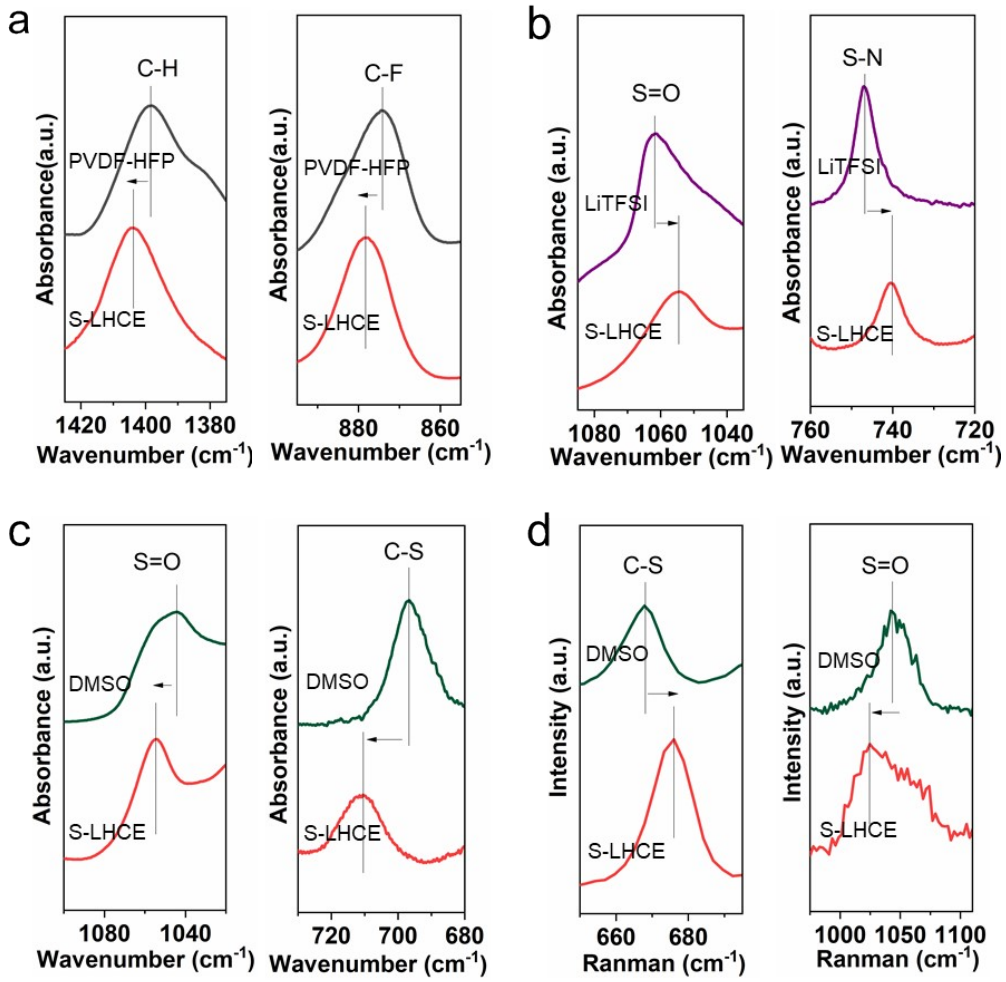

Supplementary Fig. 20. (a) ATR-FTIR of C-H and C-F (comparison of PVDF-HFP and S-LHCE). (b) ATR-FTIR of S=O and S-N (comparison of LiTFSI and S-LHCE). (c) ATR-FTIR of S=O and C-S (comparison of DMSO and S-LHCE). (d) Raman spectra of C-S and S=O (comparison of DMSO and S-LHCE).

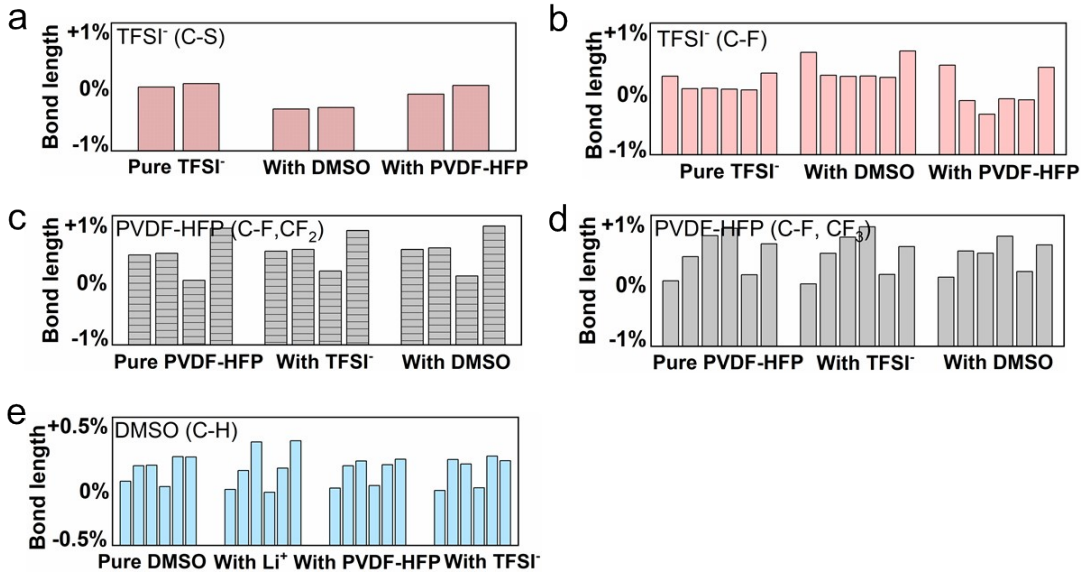

Supplementary Fig. 21. Comparison of bond length changes of chemical bonds involved in two-component systems, C-S of $TFSI^-$ (a), C-F of $TFSI^-$ (b), C-F(CF_2) of PVDF-HFP (c), C-F(CF_3) of PVDF-HFP (d), C-H of DMSO (e).

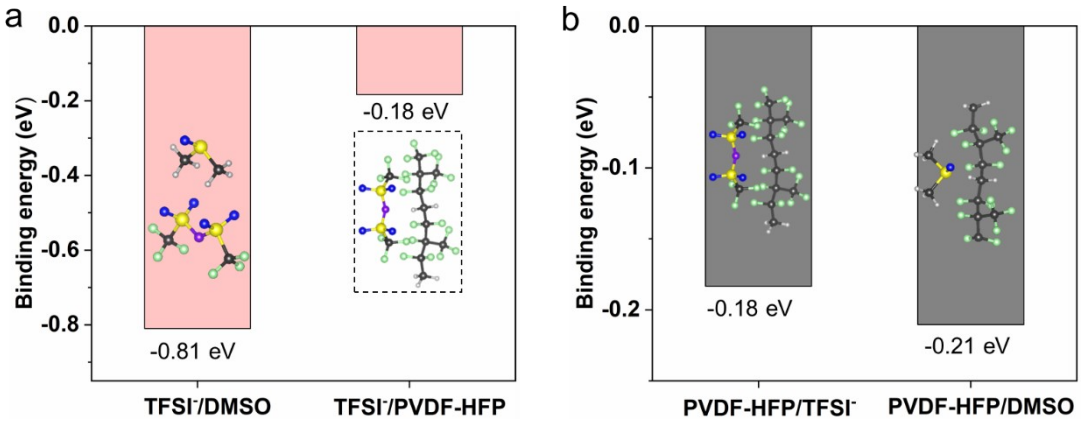

Supplementary Fig. 22. Comparison of binding energy for optimized geometric configurations of interaction systems of $TFSI^-$/DMSO and $TFSI^-$/PVDF-HFP (a), PVDF-HFP/$TFSI^-$ and PVDF-HFP/DMSO (b).

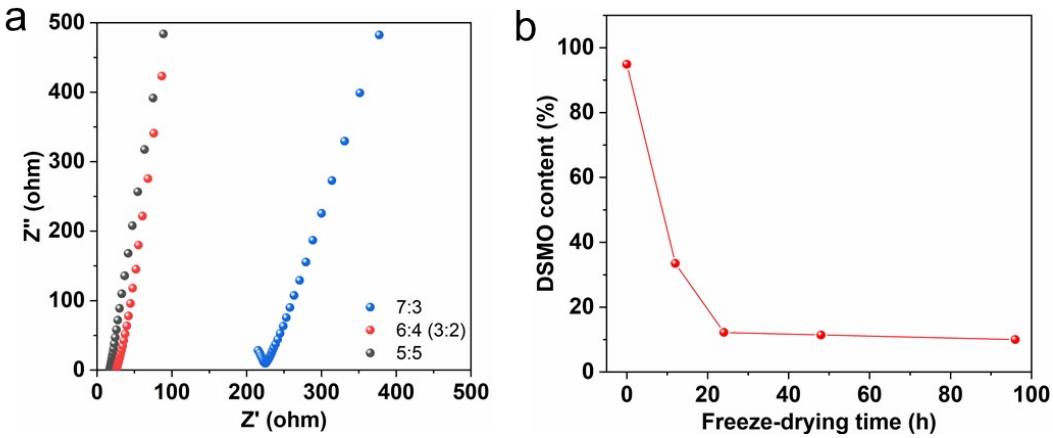

Supplementary Fig. 23. (a) Electrochemical impedance spectra of electrolytes with different LiTFSI contents. (b) Variation in DMSO content with time of freeze-drying process.

Supplementary Note: The content of LiTFSI in S-LHCE selected as 3:2 (wt.) was based on the principle of high ionic conductivity. We tested the electrochemical impedance spectroscopy with PVDF-HFP: LiTFSI of 7:3 (wt.), 3:2 (wt.) and 5:5 (wt.), respectively. As shown in Supplementary Fig. 23a, with increasing LiTFSI content, a smaller electrochemical impedance could be obtained due to more carriers. Therefore, to obtain better electrochemical performance and directly demonstrate the S-LHCE strategy, 3:2 (wt.) was selected as the weight ratio of PVDF-HFP and LiTFSI. Moreover, the content of DMSO in S-LHCE was controlled by the time of freeze-drying process. As shown in Supplementary Fig. 23b, the DMSO content remains stable in the freeze-drying time of 24-96 hours. Therefore, to quickly prepare S-LHCE with a regulated solvation structure, the time of freeze-drying process was controlled at 48 hours with a DMSO content of ~11.4 wt.%.

Supplementary Table 1. Rate performance of LFP||Li cells with different polymer electrolytes reported recently.

Polymer electrolyte	Test temperature	Current density	Discharge capacity (mAh g^{-1})
LLZO/h-polymer [6]	50 °C	0.2 C	141.4
		0.3 C	141.5
		0.5 C	143.3
		1 C	139.7
		2 C	130.8
eEPE [7]	60 °C	0.1 C	160
		0.25 C	155
		0.5 C	150
		1 C	100
PBO [8]	60 °C	0.2 C	~160
		0.5 C	~157
		1 C	~150
		2 C	~108
PLSSCQD-4/PEO [9]	60 °C	0.1 C	168
		0.2 C	158
		0.5 C	140
		1 C	133
		2 C	124
		5 C	79
PEO-LiTFSI-HAP [10]	30 °C	0.1 C	132
		0.5 C	124
		1 C	116
		3 C	89
		5 C	53
FBCPE_30 [11]	70 °C	0.1 C	162
		0.2 C	160

		0.5 C	157
		1C	150
		2C	144
5% MZ-CPE [12]	60 °C	0.1 C	154
		0.2 C	149
		0.5 C	131
		1 C	65
PLC-2PEGDE-30wt%Li [13]	60 °C	0.1 C	144.1
		0.2 C	144.5
		0.5 C	137.1
		1 C	131
LLZTO@PAN/PEO [14]	60 °C	0.2 C	146
		0.5 C	135
		1 C	98
PLLE-5% $LiNO_3$ [15]	60 °C	0.1 C	152.4
		0.2 C	151
		0.5 C	146.2
		1 C	141.4
		2 C	131.2
PAN-in situ [16]	RT	0.1 C	156.3
		0.3 C	~153
		0.7 C	~142
		1 C	~130
		2 C	112.8
es-PVDF-PEO-GDC [17]	50 °C	0.1 C	156.2
		0.2 C	152.5
		0.5 C	149.3
		1 C	145.6
		2 C	141.1

CSPE4 [18]	60 °C	0.1 C	171
		0.2 C	150
		0.5 C	125
		1 C	103
		2 C	81
		5C	40
PEE [19]	50 °C	0.2 C	145
		0.5 C	~120
		1 C	~100
		2 C	75
ICSE [20]	25 °C	0.1 C	158
		0.2 C	121
		0.5 C	82
		1 C	58
10% LLTO NTs CPE [21]	RT	0.1 C	141
		0.2 C	129
		0.5 C	118
		1 C	105
PLE [22]	25 °C	0.1 C	154.5
		0.5 C	128.1
PSE/LLZTO/PSE [23]	25 °C	0.1 C	~150
		0.5 C	130
		1 C	102
		2 C	~70
PLLE-3 [24]	25 °C	0.1 C	169.2
		0.5 C	157.2
		2 C	117.5
PVDF-HFP/SLN [25]	RT	0.1 C	156.9
		0.2 C	151.2

		0.3 C	147.7
		0.5 C	143.2
		1 C	133.2
		2 C	111.3
1 wt% I_2 + PEO [26]	50 °C	0.2 C	159
		0.4 C	153
		0.8 C	133
		1 C	111
PRX-SPE [27]	25 °C	0.1 C	159.4
		0.2 C	143.7
		0.5 C	118.9
		1 C	105.9
I-FPG [28]	45 °C	0.2 C	165.1
		0.5 C	158.2
		1 C	152.7
PBPF-O [29]	25 °C	0.1 C	153.8
		0.2 C	~153
		0.5 C	~142
		1 C	~128
		2 C	95.7
PDOL@PDA/PVDF-HFP [30]	25 °C	0.2 C	151.6
		0.5 C	~140
		1 C	~130
		2 C	~115
		3 C	~105
		4 C	~95
		5 C	~90
BC-g-PLiTFSI-b-PEGM/p [31]	RT	0.1 C	149
		0.2 C	134

		0.5 C	116
		1 C	99
		2 C	83
		5 C	61
PPL [32]	60 °C	0.1 C	163.7
		0.5 C	155.5
		1 C	152.1
		3 C	143.8
		5 C	134.4
		7 C	104.9
PEO_m-5% $Li_{25}Si_5$ [33]	45 °C	0.05 C	164.4
		0.2 C	152.8
		0.5 C	136.8
		1 C	116.3
		2 C	84.5
		4 C	47.7
	30 °C	0.1 C	~150
		0.2 C	~140
		0.3 C	~120
		0.5 C	~70
SPVDFLi-HFP50/PVDF-HFP [34]	25 °C	0.1 C	147.9
		0.2 C	138.6
		0.5 C	118.2
		1 C	98.2
Polymer-in-Ceramic [35]	25 °C	0.05 C	161
		0.1 C	160
		0.2 C	157
		0.5 C	132
		1 C	113

		1.5 C	91
Solid-LHCE	25 °C	0.2 C	159.6
		0.5C	158.9
		1 C	151.1
		2 C	138.3
		3 C	125.5
		4 C	116.9
		5 C	108.4
	50 °C	0.2 C	166.1
		0.5 C	165.2
		1C	163.8
		2 C	160.4
		3 C	157.1
		4 C	153.1
		5 C	149.2
		6 C	145.7
		7 C	142.5
		8 C	139.3
		9 C	136.4
		10 C	133.2
	100 °C	1 C	167.6
		3 C	167.1
		5 C	161.4
		8 C	155.7
		10 C	157.3
		20 C	150.9
		30 C	141.6
		50 C	102.2

References:

[1] S. Xu, Z. Sun, C. Sun, F. Li, K. Chen, Z. Zhang, G. Hou, H.-M. Cheng and F. Li, *Adv. Funct. Mater.*, 2020, **30**, 2007172.

[2] J. Paier, R. Hirschl, M. Marsman and G. Kresse, *J. Chem. Phys.*, 2005, **122**, 234102.

[3] J. P. Perdew, K. Burke and M. Ernzerhof, *Phys. Rev. Lett.*, 1996, **77**, 3865.

[4] G. Kresse and J. Furthmüller, *Phys. Rev. B*, 1996, **54**, 11169

[5] P. E. Blöchl, *Phys. Rev. B*, 1994, **50**, 17953.

[6] M. Zhang, P. Pan, Z. Cheng, J. Mao, L. Jiang, C. Ni, S. Park, K. Deng, Y. Hu and K. K. Fu, *Nano Lett.*, 2021, **21**, 7070-7078.

[7] Z. Zeng, X. Chen, M. Sun, Z. Jiang, W. Hu, C. Yu, S. Cheng and J. Xie, *Nano Lett.*, 2021, **21**, 3611-3618.

[8] J. Luo, Q. Sun, J. Liang, X. Yang, J. Liang, X. Lin, F. Zhao, Y. Liu, H. Huang, L. Zhang, S. Zhao, S. Lu, R. Li and X. Sun, *Nano Energy*, 2021, **90**, 106566.

[9] Z. Li, F. Liu, S. Chen, F. Zhai, Y. Li, Y. Feng and W. Feng, *Nano Energy*, 2021, **82**, 105698.

[10] Y. Liang, Y. Liu, D. Chen, L. Dong, Z. Guang, J. Liu, B. Yuan, M. Yang, Y. Dong, Q. Li, C. Yang, D. Tang and W. He. *Mater. Today Energy*, 2021, **20**, 100694.

[11] Y. Sun, X. Zhang, C. Ma, N. Guo, Y. Liu, J. Liu and H. Xie, *J. Power Sources*, 2021, **516**, 230686 .

[12] H. Jamal , F. Khan , S. Hyun , S. W. Min and J. H. Kim , *J. Mater. Chem. A*, 2021, **9**, 4126-4137.

[13] Q. Zeng, Y. Lu, P. Chen, Z. Li, X. Wen, W. Wen, Y. Liu, S. Zhang, H. Zhao, H. Zhou, Z.-X. Wang and L. Zhang, *J. Energy Chem.*, 2022, **67**, 157-167.

[14] W.-P. Chen, H. Duan, J.-L. Shi, Y. Qian, J. Wan, X.-D. Zhang, H. Sheng, B. Guan, R. Wen, Y.-X. Yin, S. Xin, Y.-G. Guo and L.-J. Wan, *J. Am. Chem. Soc*., 2021, **143**, 5717-5726.

[15] Z. Zhang, J. Wang, S. Zhang, H. Ying, Z. Zhuang, F. Ma, P. Huang, T. Yang, G. Han and W.-Q. Han, *Energy Storage Mater.*, 2021, **43**, 229-237.

[16] M. Yao, Q. Ruan, T. Yu, H. Zhang and S. Zhang, *Energy Storage Mater.*, 2022, **44**, 93-103.

[17] L. Gao, S. Luo, J. Li, B. Cheng, W. Kang and N. Deng, *Energy Storage Mater.*, 2021, **43**, 266-274.

[18] P. N. Didwal, Y. N. Singhbabu, R. Verma, B.-J. Sung, G.-H. Lee, J.-S. Lee, D. R. Chang and C.-J. Park, *Energy Storage Mater.*, 2021, **37**, 476-490.

[19] C. Zhang, Z. Niu, J. Bae, L. Zhang, Y. Zhao and G. Yu, *Energy Environ. Sci*., 2021, **14**, 931-939.

[20] J. Yuan, R. Dong, Y. Li, Y. Liu, Z. Zheng, Y. Liu, Y. Sun, B. Zhong, Z. Wu and X. Guo, *Chem. Commun.*, 2021, **57**, 13004-13007.

[21] L. Xu, L. Zhang, Y. Hu and L. Luo, *Chem. Commun.*, 2021, **57**, 11068-11071.

[22] G. Bai, N. Liu, C. Wang, W. Wei, X. Liu, Y. Li, *Chem. Commun.*, 2021, **57**, 11493-11496.

[23] Y.-N. Yang, F.-L. Jiang, Y.-Q. Li, Z.-X. Wang and T. Zhang, *Angew. Chem., Int. Ed*., 2021, **60**, 24162-24170.

[24] K. He, S. H.-S. Cheng, J. Hu, Y. Zhang, H. Yang, Y. Liu, W. Liao, D. Chen, C. Liao, X. Cheng, Z. Lu, J. He, J. Tang, R. K. Y. Li and C. Liu, *Angew. Chem., Int. Ed.*, 2021, **60**, 12116-12123.

[25] S. Xia, B. Yang, H. Zhang, J. Yang, W. Liu and S. Zheng, *Adv. Funct. Mater.*, 2021, **31**,

2101168.

[26] O. Sheng, H. Hu, T. Liu, Z. Ju, G. Lu, Y. Liu, J. Nai, Y. Wang, W. Zhang and X. Tao, *Adv. Funct. Mater.*, 2021, 2111026.

[27] J. Seo, G.-H. Lee, J. Hur, M.-C. Sung, J.-H. Seo and D.-W. Kim, *Adv. Energy Mater.*, 2021, **11**, 2102583.

[28] Y. Lin, M. Wu, J. Sun, L. Zhang, Q. Jian and T. Zhao, *Adv. Energy Mater.*, 2021, **11**, 2101612.

[29] S. Zhang, T. Liang, D. Wang, Y. Xu, Y. Cui, J. Li, X. Wang, X. Xia, C. Gu and J. Tu, *Adv. Sci.*, 2021, **8**, 2003241.

[30] D. Chen, M. Zhu, P. Kang, T. Zhu, H. Yuan, J. Lan, X. Yang and G. Sui, *Adv. Sci.*, 2022, **9**, 2103663.

[31] M. Zhou, R. Liu, D. Jia, Y. Cui, Q. Liu, S. Liu and D. Wu, *Adv. Mater.*, 2021, **33**, 2100943..

[32] Z. Wang, L. Shen, S. Deng, P. Cui and X. Yao, *Adv. Mater.*, 2021, **33**, 2100353.

[33] Y. Liu, R. Hu, D. Zhang, J. Liu, F. Liu, J. Cui, Z. Lin, J. Wu and M. Zhu, *Adv. Mater.*, 2021, **33**, 2004711.

[34] X. Liu, J. Liu, B. Lin, F. Chu and Y. Ren, *ACS Appl. Energy Mater.*, 2022, **5**, 1031.

[35] S. Yu, Q. Xu, X. Lu, Z. Liu, A. Windmüller, C.-L. Tsai, A. Buchheit, H. Tempel, H. Kungl, H.-D. Wiemhöfer and R.-A. Eichel, *ACS Appl. Mater. Interfaces*, 2021, **13**, 61067-61077.